

Unstructured Finite Element Mesh Decimation for Real-Time Hurricane Storm Surge Forecasting

Matthew V. Bilskie^a, Scott C. Hagen^{a,b,c}, Stephen C. Medeiros^d

^a*Louisiana State University, Center for Coastal Resiliency, 124B Sea Grant Hall, Baton Rouge, LA 70803*

^b*Louisiana State University, Department of Civil and Environmental Engineering*

^c*Louisiana State University, Center for Computation and Technology*

^d*Embry-Riddle Aeronautical University, Department of Civil Engineering, 1 Aerospace Blvd, Daytona Beach, FL 32114*

Abstract

A previously developed research-grade (e.g. high-resolution) unstructured mesh of the northern Gulf of Mexico (named NGOM3) is optimized to produce a computationally efficient forecast-grade mesh for deployment in a real-time hurricane storm surge early warning system. The real-time mesh is developed from a mesh decimation scheme with focus on the coastal floodplain. The mesh decimation scheme reduces mesh nodes and elements from the research-grade mesh while preserving the representation of the bare-earth topography. The resulting real-time unstructured mesh (named NGOM-RT) contains 64% less mesh nodes than the research-grade mesh. Comparison of (ADCIRC+SWAN) simulated times-series and peak water levels to observations between the research-grade and real-time-grade meshes for Hurricanes Ivan (2004), Dennis (2005), Katrina (2005), and Isaac (2012) show virtually no difference. Model simulations with the NGOM-RT mesh are 1.5-2.0 times faster than using NGOM3 on the same number of compute cores.

Keywords: Storm Surge, Unstructured Mesh, Mesh Decimation, Coastal Flooding

Email address: mbilsk3@lsu.edu (Matthew V. Bilskie)

1. Introduction

The northern Gulf of Mexico (NGOM) experiences frequent hurricanes that can generate large storm surges resulting in coastal floods and are among the costliest and deadliest natural disasters [1]. This region has been affected by numerous recent storms such as Hurricanes Ivan (2004), Dennis (2005), Katrina (2005), Rita (2005), Gustav (2008), Ike (2008), Isaac (2012), Hermine (2016), Harvey (2017), Irma (2017), Nate (2017), and Michael (2018). Accurate forecasting of peak water levels and overland inundation is useful in order to prepare for such events, mitigate property damage, and limit loss of life [2, 3]. Numerical computer models can be used to predict the flood location, timing, magnitude, and duration. Such predictions are used by a variety of local, regional and federal institutions in order to design evacuation strategies, activate floodgates and surge barriers, and aid in post-disaster recovery operations.

In the past decade, physics-based numerical models that compute water levels and velocities for astronomic tides and tropical cyclone-driven storm surges have improved, particularly with the development of new data collection technology (e.g. lidar) and readily available high-performance computational resources. With these enhanced technologies, the focus has been on developing models with finer spatial and temporal resolution. Finer resolution allows for enhanced representation of the landscape, specifically topography, bathymetry, raised features, and vegetation [4–8]. In addition, advancements have been made in improving the physics via tight-coupling of wind-wave models to storm surge models [9–14] and improved tropical cyclone wind drag formulations [15–17, 11]. Such advancements have increased model accuracy of hurricane-driven water levels and related overland inundation across coastal floodplains.

Numerical hurricane storm surge models are now deployed in real-time and results are being adopted by emergency managers and stakeholders in their decision-making framework [18, 19]. Even with the advancements and availability of computational power, applying physics-based storm surge models that are highly descriptive of topographic and bathymetric features in real-time is a challenge. First and foremost, the storm surge simulation for a particular forecast must be performed (and results disseminated to end-users) faster than actual time - in most cases the simulation must be performed in a fraction of actual time (total simulation time on the order of 1-2 hr). Second, the total number of available computational cores for a

given high performance computer (HPC) is likely to be limited. In addition, the size of the model domain and level of resolution must be large and fine enough, respectively, to cover a wide-range of possible hurricanes [10]. Therefore, a balance must be achieved in the level of model detail (i.e. resolution and region of interest) and simulation turnaround time. This leads to the question of how to discretize a model domain with sufficient detail so that it can run in a reasonable time frame and produce storm surge results that can be specifically used by emergency managers in near real-time.

Many studies have developed methods to semi-automate the mesh generation and others have aimed at strategically placing computational points within the model domain to minimize model error [20–22]. For example, Hagen et al. [23] developed mesh size functions based on *a posteriori* results from an astronomic tide simulation using localized truncation error analysis (LTEA). They found that LTEA created a superior unstructured mesh for astronomic tide modeling than wavelength to mesh size-based meshing criteria [24]. These methods have been expanded to include non-linear terms of the shallow water equations and have been successfully implemented for large and complex domains [25–29]. Recent techniques in automated mesh generation for shallow water flow models have been developed to consider minimal inputs (shoreline and elevation data) to generate a quality unstructured mesh using signed distance functions and force-balance algorithms to guide mesh sizing criteria [30–32].

The methods mentioned above have been proven to work well in coastal waters (where a depth of water is consistently maintained), but little work has been performed to create quality and computationally efficient unstructured meshes across the coastal floodplain (normally dry areas) that become inundated at high tide or during storm surge events. Coastal floodplains are complex landscapes that contain sharp gradients in elevation and a variety of natural and urbanized landscape features [33, 5]. Furthermore, the process of an advancing or receding flood wave is a modeling challenge [34]. Typical methods of mesh generation across the landscape attempt to resolve significant terrain features (e.g. levees, floodwalls, ridges, bayous) that can inhibit or conduct flows [4, 35]. Such methods are useful in developing more topographically accurate meshes, but do little to guide the mesh generation process in terms of local mesh sizing. Therefore, mesh resolution is determined from the mesh creator’s intuition and experience selecting a minimum element size to achieve a selected minimum time step along with the computational resources available. This procedure often results in over-resolved

meshes because the spatial variability of terrain is not included in the mesh generation process [4].

The goal of this study is to develop a detailed unstructured finite element mesh with specific focus on the Mississippi, Alabama, and Florida panhandle coastal floodplain for use in a real-time storm surge modeling framework. To achieve this goal we adopt a mesh decimation technique to relax local mesh element sizes while preserving the geometric accuracy of the coastal floodplain as represented by the mesh and its solution of the shallow water equations. This ultimately leads to a mesh that can be run efficiently and therefore employed in the real-time storm surge forecasting framework.

The paper is organized in the following manner. The hydrodynamic model is described as well as the algorithms employed to adjust local element sizes, including mesh decimation. The results of these techniques are presented along with simulation results, including validation, for Hurricanes Ivan (2004), Dennis (2005), Katrina (2005), and Isaac (2012). In addition, the compute time for simulations employing the research-grade vs. real-time unstructured meshes are shown. The paper concludes with a summary and future research.

2. Methods

2.1. ADCIRC+SWAN Model

The tightly coupled advanced circulation (ADCIRC) and simulating waves nearshore (SWAN) models were used to simulate hurricane-driven coastal circulation and overland inundation. ADCIRC solves for water surface elevations and depth-averaged velocities across an unstructured finite element mesh using a modified form of the shallow water equations, specifically the generalized wave continuity equation and depth-averaged momentum equations [36–39]. In this study, the ADCIRC time-step is 1.0 second to satisfy the Courant number criteria and the implicit solver was used. Surface roughness parameters are based on the Coastal Change Analysis Program (C-CAP) land use land cover (LULC) (<http://www.csc.noaa.gov/>) [11, 4]. Hydraulic bottom friction was parameterized via spatially-varying Mannings n coefficients and vegetation canopy was parameterized by surface directional roughness lengths [40] and a canopy coefficient that limits the winds ability to transfer momentum to the water surface in dense canopies [39]. Offshore Mannings n values were assigned based on the bottom sediment type [41] and local depth [42–44].

SWAN is a phase-averaged wave model that solves the action balance equation for relative frequency and wave direction, which evolves in geographical space, spectral space, and time across an unstructured finite element mesh [45, 12, 46, 47]. Simulated wave frequencies were discretized logarithmically into 40 frequency bins ranging from 0.31384 to 1.420416 Hz and directions into 36 10° bins. Wind inputs and wind-induced wave growth were based on Cavaleri and Rizzoli [48] and Komen et al. [49] with modified whitecapping updated by Rogers et al. [50]. Bottom roughness was converted from Mannings n to roughness lengths [11, 51]. Depth-induced wave breaking was equal to 0.73 based on Battjes and Janssen [52]. A spectral propagation velocity limiter was included to limit false wave refraction in regions with coarse mesh resolution away from the study area [13].

The ADCIRC+SWAN model are tightly-coupled and operate on the same unstructured finite element mesh. ADCIRC passes water levels and depth-averaged currents to SWAN. SWAN then computes wave radiation stress gradients that are passed to ADCIRC. This occurs every 600 seconds, which is also the SWAN time step.

2.2. Unstructured Finite Element Mesh Development

The development of the real-time unstructured mesh (named NGOM-RT, RT for real-time) begins with the high-resolution, research-grade, NGOM3 unstructured finite element mesh [42]. We refer to NGOM3 as a "research-grade" mesh because it is the culmination of more than a decade of our efforts to provide the most detailed description of the northern Gulf to-date [4, 5, 53, 42, 54, 35, 55–60]. The NGOM3 mesh consists of 5.5 million nodes and spans the western north Atlantic Ocean (from the 60° west Meridian), Caribbean Sea, and Gulf of Mexico with focus on the Mississippi, Alabama, and Florida panhandle coastal floodplain up to the 15 m elevation contour. It was developed to provide the most complete description of tide and surge dynamics in this region with nominal concern for computational cost. With its highly descriptive properties and extensive validation it serves as a benchmark of comparison for any subsequent efforts.

The NGOM3 computational mesh serves as a starting point to create a real-time mesh via the reduction of mesh elements. This was accomplished through the five steps, described in detail in the following sections and outlined in Figure 1.

1. Mesh nodes and elements in the nearshore portion (e.g. sounds, estuary,

- 148 bays, and rivers) of the study domain were extracted from the NGOM3
149 mesh.
- 150 2. Mesh nodes were reduced in the open ocean through localized trunca-
151 tion error analysis (LTEA).
 - 152 3. The upland model domain was trimmed to remove regions of high to-
153 pography that are unlikely to become inundated from a tropical cy-
154 clone.
 - 155 4. A mesh decimation algorithm was employed to determine regions where
156 the mesh can be coarsened while still preserving the terrain.
 - 157 5. Vertical feature lines were extracted.
 - 158 6. An advancing front paving algorithm was employed to generate an un-
159 structured mesh of the coastal floodplain based on the vertical features
160 and mesh size function.
 - 161 7. Elevations from a high-resolution digital elevation model (DEM) were
162 interpolated to the mesh nodes.

163 *2.2.1. Nearshore and Inland Waterways*

164 The research-grade NGOM3 mesh includes high-resolution along the
165 shoreline (20 - 100 m element size) in the nearshore areas of Mississippi,
166 Alabama, and the Florida panhandle. The resolution and mesh topology for
167 this area will be preserved. Mesh resolution in the nearshore is constrained
168 by the width of the smallest water body features that must be included in the
169 model. For this work, water-body features (inlets, rivers, and Intracoastal
170 Waterway) that have a width greater than 100 m are included so at least
171 three elements with spacing of 20 - 40 m can span their respective width.
172 This is to ensure that, at a minimum, these bathymetric features are repre-
173 sented by the mesh as a trapezoidal cross-section. Away from the water-body
174 features, the nearshore area was defined as the 3 m (NAVD88) depth contour
175 in Mississippi and Alabama and out to the 20 m (NAVD88) depth contour
176 along the Florida panhandle.

177 *2.2.2. Localized Truncation Error Analysis*

178 The unstructured finite element mesh for water-only regions spanning
179 the western north Atlantic (WNAT) model domain (western north Atlantic,
180 Caribbean Sea, and Gulf of Mexico) was generated using localized truncation
181 analysis with complex derivatives (LTEA+CD) [28]. The goal of LTEA+CD

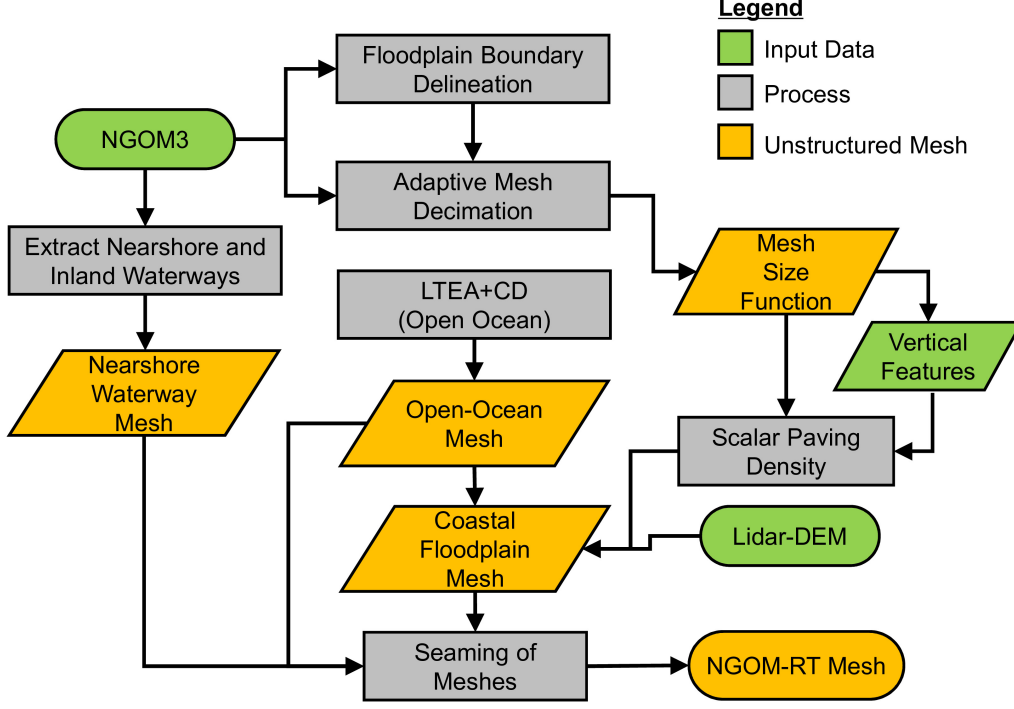


Figure 1: Flowchart outlining the unstructured mesh generation process that stems from the high-resolution NGOM3 and previously developed lidar-derived DEM and vertical features [5, 4].

is to evenly distribute local truncation errors across the entire model domain by relaxing the mesh resolution in areas where truncation errors are low [29, 26, 25, 61, 56, 28]. The result of LTEA+CD is a spatially varying elemental size function. A mesh paving algorithm is then used to create the unstructured finite element mesh by using the LTEA+CD-generated node spacing requirements [26]. The LTEA+CD localized truncation error of linear Galerkin finite elements is:

$$\hat{\tau}_{ME}^+ = \frac{\Delta^6}{1440} \underbrace{[\omega(i\hat{v}_0 - \hat{u}_0) + (\tau\hat{v})_0 + i(\tau\hat{u})_0 - i(f\hat{v})_0 + (f\hat{u})_0]}_{\text{derivative term}}^6 \quad (1)$$

189 where Δ is the distance from the central node to that of any of its neighbors,
 190 ω is tide constituent frequency, \hat{u} and \hat{v} are the complex velocities in the x-
 191 and y-direction, respectively, τ is the bottom stress, and f is Coriolis force
 192 [29]. Target local element sizes obtained from Equation 1 are rearranged
 193 into the form of $\Delta^* = aD$, where a is an arbitrary scale factor and D is
 194 a deterministic scale factor. A uniform scale factor was used to indirectly
 195 limit the gradient in the target element size and D was applied based on a
 196 Gaussian distribution to smooth the gradient in target element sizes [27, 29].
 197 A maximum element size gradient of 0.75 was used, which limits adjacent
 198 elements to being no larger than a factor of 2 in elemental area (big/small).

199 We begin with an arbitrary and generally spatially uniform high-
 200 resolution mesh (Figure 3A) of the WNAT model domain with bathymetric
 201 elevations derived from SRTM_30 [62]. The mesh contains 456,000 nodes
 202 and 900,000 elements with local element sizes ranging from 300 m to 25 km.
 203 The mesh was included in a fully non-linear 90-day ADCIRC simulation (5.0
 204 second time step), including advection, Coriolis force, and quadratic bottom
 205 friction. The model was forced with seven tidal constituents along the open
 206 ocean boundary (K1, O1, M2, S2, N2, K2, and Q1). Water levels and depth-
 207 averaged currents were resynthesized from the last 45 days of simulation and
 208 used as inputs into LTEA+CD. Target element sizes were computed for 23
 209 individual tidal constituents at each mesh node and the minimum value was
 210 selected to generate the final target element size for the WNAT model do-
 211 main. This process was repeated for a second iteration, with the input mesh
 212 being the output mesh of the first iteration.

213 *2.2.3. Floodplain Boundary Delineation*

214 The NGOM3 model includes normally dry regions up to the 15 m eleva-
 215 tion contour across Mississippi, Alabama, and the Florida panhandle. The
 216 high upland elevation contour was necessary as the NGOM3 model was used
 217 to study the dynamics of coastal flooding under future sea level rise scenarios.
 218 Since a 15 m storm tide is unlikely in this region under present-day condi-
 219 tions, portions of the upper floodplain were removed from the mesh to reduce
 220 the number of computational points. A maximum of maximums (MOM) wa-
 221 ter level surface was derived from NGOM3 ADCIRC+SWAN simulations
 222 forced by 219 synthetic storms computed from Bilskie et al. [63]. The final
 223 upload boundary is the extent of the MOM boundary plus a 500 m buffer.
 224 The boundary generally follows the 10-15 m elevation contour in Mississippi
 225 and Alabama and the 5 m elevation contour along the Florida panhandle.

226 *2.2.4. Adaptive Mesh Decimation*

227 Mesh decimation provides a means to coarsen mesh node density in cer-
 228 tain regions of the domain. This can be accomplished through input geome-
 229 try, solution gradients, visual appearance, and error functions. Edge collapse
 230 is one common mesh decimation algorithm. The edge collapse algorithm con-
 231 sideres a target element edge between two mesh nodes, relocates each mesh
 232 node to the same location, connects the incident edges to one of the mesh
 233 nodes, removes the other mesh node, and removes mesh elements that have
 234 disjoint nodes (Figure ??) [64, 65].

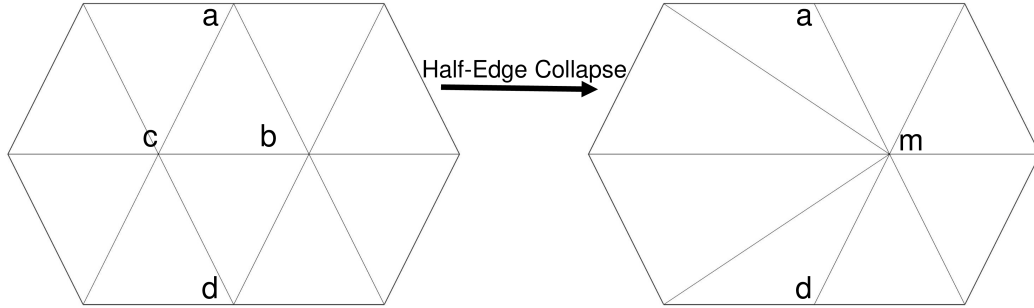


Figure 2: Example of half-edge collapse. Mesh node c is removed and becomes mesh node m and incident edges (a - c and d - c) are removed. Then disjoint node c is removed.

235 In this work, mesh decimation is applied to the overland regions of the
 236 NGOM3 unstructured finite element mesh. Recall that the mesh represents a
 237 large set of bare-earth elevations for given latitudes and longitudes. The goal
 238 is to approximate the terrain represented by the denser mesh with a lower
 239 resolution mesh by removing nodes that do not increase the approximation
 240 error above a given threshold [66]. Typically, nodes can be removed until
 241 either 1) a set number of mesh elements or nodes are achieved, 2) a global
 242 error threshold is met or 3) a combination of 1 and 2.

243 We employed Matlab's *reducepatch* algorithm for mesh decimation. The
 244 input was the unstructured mesh of the NGOM3 coastal floodplain from Mis-
 245 sissippi to Florida's Big Bend region (containing 3,002,723 mesh elements).
 246 A mesh element threshold of 450,000 was used to reduce the total number
 247 of mesh elements by 85%. The value of 450,000 was obtained based on an
 248 iterative process through visual inspection of the decimated mesh's repre-
 249 sentation of the topography. Matlab's *reducepatch* algorithm was selected
 250 because of its ease of use of use to perform mesh decimation as well as its

251 speed. Unfortunately, detailed information regarding the *reducepatch* func-
 252 tion is not publicly available. A drawback of implementing the *reducepatch*
 253 mesh decimation is that mesh quality is not preserved. Therefore, a spatially
 254 varying mesh size function was based only on the decimated mesh (Figure
 255 1).

256 2.2.5. Vertical Features

257 Vertical features are defined as linear raised or sunken bare-earth terrain
 258 features that can impact the path, pattern, and magnitude of flooding. Ver-
 259 tical features are typically long and narrow with respect to the desired local
 260 element size and are substantially higher in elevation than the surrounding
 261 terrain. Examples of vertical features include raised railroads and roadbeds,
 262 flood walls, levees, and natural ridges. Because the width (w) of these fea-
 263 tures are narrow compared to the local element size ($w_{vf} \ll \Delta$) their width
 264 scales cannot be adequately represented by the unstructured mesh without
 265 drastically decreasing the local element size. Therefore, vertical features re-
 266 quire special treatment during the mesh generation process.

267 This work takes advantage of the vertical features previously developed
 268 by Bilskie et al. [4]. A short summary is provided, but for algorithm de-
 269 tails, parameters, and psuedo-code please refer to Bilskie et al. [4]. Vertical
 270 features were semi-automatically generated and based on the delineation of
 271 small watersheds from a bare earth-lidar-derived DEM. The watershed lines
 272 and DEM were then examined to relate the watershed line elevations with
 273 respect to the surrounding terrain. Vertical features were extracted from the
 274 watershed line if they met certain metrics with respect to length, height, and
 275 width. The extracted vertical features were then compared to the mesh size
 276 function generated from the decimated mesh. Final cleaning of the extracted
 277 feature lines involved removing lines that are shorter and too close together
 278 compared to the local element size.

279 2.2.6. Coastal Floodplain Mesh Generation - Scalar Paving Density

280 An unstructured mesh of the coastal floodplain was generated using an
 281 advancing front paving algorithm [67, 68] within the Surface Water Modeling
 282 System (SMS) [69]. The inputs to the paving algorithm include 1) a polygon
 283 of the model domain (exterior constraints), 2) vertical feature lines (interior
 284 constraints), and 3) mesh size function. The paving algorithm attempts to
 285 create mesh elements similar in size to those prescribed by the size function
 286 while also preserving mesh quality. In addition, elements were inserted so

287 their edges align with vertical feature lines where present. The paving process
288 was performed for 43 sub-domains that make up the desired coastal floodplain
289 portion of the model domain. Finally, the LTEA-driven mesh for the open
290 ocean and waterways was seamed with the mesh of the coastal floodplain
291 and inland waterways.

292 *2.2.7. Bathymetry and Topography*

293 A seamless digital elevation model (DEM) for the nearshore and coastal
294 floodplain regions was generated from the latest and best-available bathymet-
295 ric and topographic data [42]. Bathymetric data included National Ocean
296 Service (NOS) hydrographic surveys ([http://www.ngdc.noaa.gov/mgg/
297 bathymetry/hydro.html](http://www.ngdc.noaa.gov/mgg/bathymetry/hydro.html)), US Army Corps of Engineers submerged channel
298 surveys and river cross sections and boat-mounted depth sounder surveys.
299 Elevation data were obtained from recent airborne bare-earth lidar provided
300 by the Northwest Florida Water Management District, NOAA Digital Coast,
301 Coastal Topographic Lidar (<http://coast.noaa.gov/digitalcoast>), NASA Ex-
302 perimental Advanced Airborne Research Lidar (EAARL) system, and Joint
303 Airborne Lidar Bathymetry Technical Center of Expertise (JALBTCX)
304 CHARTS system. All elevations not referenced to NAVD88 were converted to
305 NAVD88 using NOAA’s VDatum (<https://vdatum.noaa.gov/>). Additional
306 details on the development of the seamless DEM can be found in Bilskie et al.
307 [42] and Bilskie et al. [4], and Bilskie and Hagen [5].

308 The seamless DEM was interpolated to the unstructured mesh using the
309 cell area averaging method of Bilskie and Hagen [5], but with a 2x smooth-
310 ing criteria (<https://github.com/mattbilskie/DEM2GRD>). Smoothing was
311 done to ensure that the mesh represented the coastal landscape while re-
312 laxing steep elevation gradients across a single element. The shallow-water
313 equations are not intended to resolve large flow gradients (i.e. turbulence)
314 and their presence can lead to numerical instabilities.

315 *2.2.8. Additional Mesh Modifications*

316 Alongside the development of the NGOM3 mesh, flood protection infras-
317 tructure (e.g. levees and floodwalls) across the Louisiana coast has also been
318 meshed [9]. Although the scope of the current modeling study does not focus
319 on Louisiana, areas of southeastern Louisiana (east of the Mississippi River
320 levee) are included in the unstructured mesh. These areas are included to
321 allow surge to propagate and attenuate across the floodplain rather than in-
322 cluding a no-flow boundary condition at the shoreline. The ADCIRC mesh

323 developed for the 2012 Louisiana Coastal Master Plan was used for regions
324 east of the Mississippi River [70], including the model description of the
325 flood protection infrastructure. In addition, the NGOM-RT includes a wave
326 radiation boundary condition to include flows in the Mississippi River.

327 *2.3. Model Forcing*

328 The NGOM3 and NGOM-RT models were forced by astronomic tides
329 along the open ocean boundary located at the 60° west meridian (K1, O1,
330 M2, S2, N2, K2, and Q1) as derived from the Oregon State TPXO7.2 tidal
331 atlas [71, 72]. Due to the large model domain tidal potential was also included
332 for the same tidal constituents. Each simulation began as a cold-start and
333 the astronomic tides were ramped up by a hyperbolic function over the course
334 of 7 days, followed by an addition 7 days of dynamic steady state (tide spin-
335 up). The NGOM-RT model was also forced with a constant river flow of
336 4,730 cubic meters per second to represent average conditions during the
337 hurricane season for the Mississippi River at Baton Rouge.

338 The storm surge simulations were hot-started from the tide spin-up sim-
339 ulation. Wind and pressure fields were developed using a blend of modeled
340 winds and objectively analyzed measurements as outlined by Bunya et al.
341 [9] and Bilskie et al. [42]. Ivan, Dennis, and Katrina were based on NOAA’s
342 H*WIND (Hurricane Research Division Wind Analysis System) [73] for the
343 core of the storm and then blended with Gulf-scale winds from the IOKA (In-
344 teractive Objective Kinematic Analysis) system [74]. The core of Hurricane
345 Isaac was modeled by the latest version of the TC96 mesoscale model [75].
346 Thirty minute sustained marine-based winds at 10 m height were applied to
347 the ADCIRC simulation every 15 minutes. To include wind reduction due to
348 above ground obstacles the ADCIRC model used directional wind reductions
349 (every 30°) derived from NOAA CCAP land use land cover data [42].

350 *2.4. Measurements and Evaluation of Model Performance*

351 Measurements include observations of time-series water levels and high
352 water marks (HWM). Time-series water levels for each hurricane event were
353 obtained from NOAA tide gages, US Army Corps of Engineers (USACE)
354 water level stations, and USGS gages. Prior to Hurricane Isaac the USGS
355 deployed over 60 temporary gages around the predicted impact zone. Most of
356 the gages were placed on normally dry land. In addition to time-series water
357 levels, model results were compared to measured HWMs obtained from the

358 Federal Emergency Management Agency (FEMA) and NOAA. A list of all
 359 observation stations and data source agencies can be found in Table 1.

360 For each hurricane event model performance is evaluated by comparing
 361 simulated results to measured data using scatter index (SI):

$$SI = \frac{\sqrt{\frac{1}{N} \sum_{i=1}^N (E_i - \bar{E})^2}}{\frac{1}{N} \sum_{i=1}^N |O_i|} \quad (2)$$

362 and bias:

$$bias = \frac{\frac{1}{N} \sum_{i=1}^N E_i}{\frac{1}{N} \sum_{i=1}^N |O_i|} \quad (3)$$

363 where N is the number of measurements, $E_i = S_i - O_i$, S is the simulated
 364 water level, and O is the observed water level [7]. Water level stations that
 365 had erroneous data, influence of rainfall runoff, or lacked a defined peak were
 366 omitted.

367 Observed HWM were assessed and measurements that contained error,
 368 included wave runup, river discharges, or rainfall runoff effects were dis-
 369 carded [76]. Additionally, HWMs that contained simulated errors outside
 370 the interquartile range (IQR) were removed from the analysis:

$$E_i < Q_1 + 1.5 * IQR \quad (4)$$

$$E_i > Q_3 + 1.5 * IQR \quad (5)$$

372 where Q_1 and Q_3 are the first and third quartiles and $IQR = Q_3 - Q_1$. The
 373 error at each HWM is $E_i = S_i - O_i$. The method of using IQR for the removal
 374 of HWMs is common among storm surge validation studies [9, 11, 42].

375 In addition, simulated peak water levels between each model were quan-
 376 tified using root mean square (RMS) difference at the mesh nodes:

$$RMS = \sqrt{\frac{1}{N} \sum_{i=1}^N (\eta_F - \eta_C)^2} \quad (6)$$

377 where η_F and η_C are the simulated peak water levels from the fine (NGOM3)
 378 and coarse (NGOM-RT) mesh solutions.

379 3. Results

380 3.1. Localized Truncation Error Analysis

381 The local element size of the initial high-resolution mesh of the WNAT
382 is compared to the first and second iteration of the LTEA-derived meshes
383 (Figure 3). In general, mesh resolution is coarsened in the deeper waters of
384 the Gulf of Mexico, Caribbean Sea, and western Atlantic and high resolution
385 exists at regions of large bathymetric gradients (e.g. the continental shelf
386 and Bahamas Bank), shallow depths, and the shoreline. Approximately 25%
387 of the model domain includes element spacing less than 10 km for both
388 LTEA-derived meshes in contrast to 86% of the initial mesh (Figure 4). This
389 indicates that much of the total area of the model domain is over-resolved
390 in the initial mesh for a real-time storm surge application. Specifically, the
391 deep waters are over-resolved and hydrodynamically important geophysical
392 features such as the continental shelf (specifically along the U.S. east coast)
393 are under-resolved.

394 The first iteration of LTEA+CD results in spatially varying element sizes
395 ranging from 0.1 - 45 km and a total node count of 215,231. Areas along
396 the northern Gulf of Mexico include the highest resolution on the order of 1
397 km followed by the the Bahamas Bank at 4 - 5 km resolution (Figure 3C-D).
398 Element spacing is generally around 7 - 9 km on the continental shelf and
399 rapidly increases to 15 km and greater towards deeper water.

400 The second and final iteration of LTEA+CD yields a range of element
401 sizes from 0.1 - 70 km with a total node count of 595,921 (Figure 4E-F). High
402 resolution is retained along the northern Gulf of Mexico coast; however, ele-
403 ment spacing across the Bahamas Bank and on the continental shelf varies as
404 compared to the first iteration. In addition, mesh resolution rapidly reduces
405 to greater than 30 km from the continental shelf to the deep ocean and by
406 as much as 70 km in the Atlantic (west of Bermuda).

407 3.2. Adaptive Mesh Decimation and Scalar Paving Density

408 Mesh decimation across the coastal floodplain, using the high-resolution
409 NGOM3 model as the input, results in fewer nodes and elements. For the full
410 floodplain region of interest, the original mesh included 1,561,493 nodes and
411 3,002,723 elements and the decimated mesh reduced the count to 276,569
412 nodes and 450,000 elements for a node and element count reduction of 82%
413 and 85%, respectively (recall the constraints set on the mesh decimation were
414 to reduce the total element count by 85%). Figure 5 shows an example of the

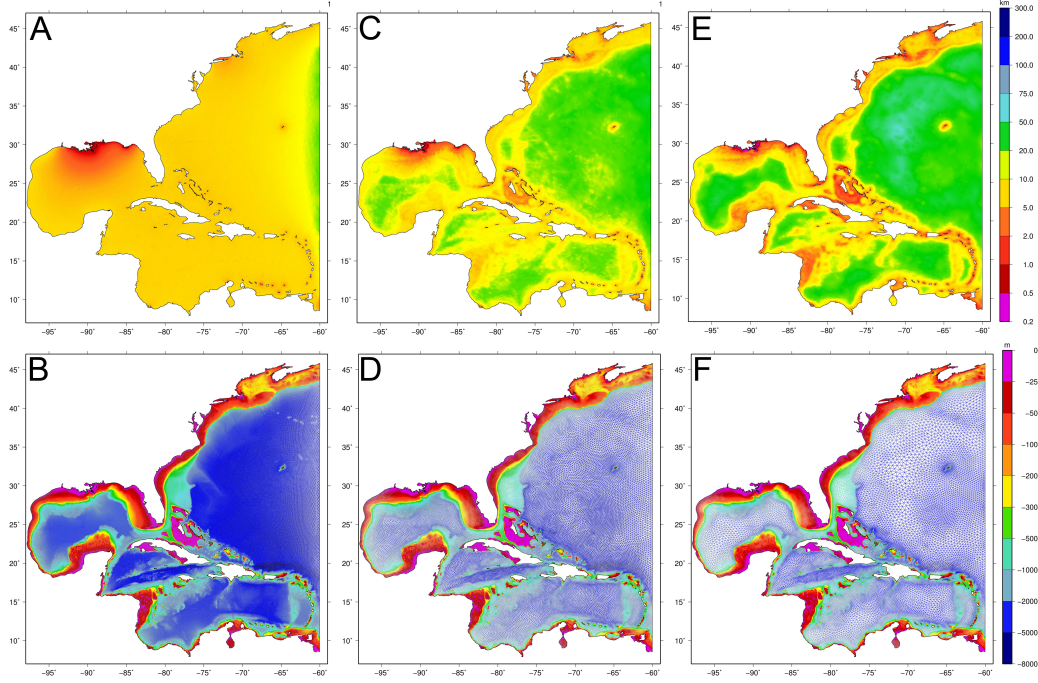


Figure 3: A) Local element size (km) and B) bathymetry (m) for the initial mesh to be used for LTEA (457k nodes). C) Local element size resulting from the first iteration of LTEA (215k nodes) and the D) resulting mesh and bathymetric representation. E) Local element size for the mesh obtained from the second iteration of LTEA (596k nodes) and the F) resulting mesh and bathymetric representation.

415 mesh decimation procedure for a region in Pascagoula, MS (adjacent to the
 416 Escatawpa River). The original high-resolution mesh of this area contains
 417 local element sizes of 50 m (Figure 5A-B) and describes the overland topog-
 418 raphy with high detail (Figure 5C). Vertical features in this region include
 419 Interstate 10 (spanning east-west to north) and U.S. 90 (spanning southwest-
 420 northeast). The decimated mesh (Figure 5D) yields a coarser node density
 421 and larger elements ranging from 100 - 300 m (Figure 5E). The description of
 422 the topography is retained with the decimated mesh, specifically the vertical
 423 features (Figure 5F). However, visual inspection indicates that mesh quality
 424 is compromised (Figure 5D).

425 The result of scalar paving density using the local element spacing from
 426 the decimated mesh (Figure 5E) and vertical feature lines is a mesh with
 427 similar resolution as the decimated mesh, but with enhanced element quality

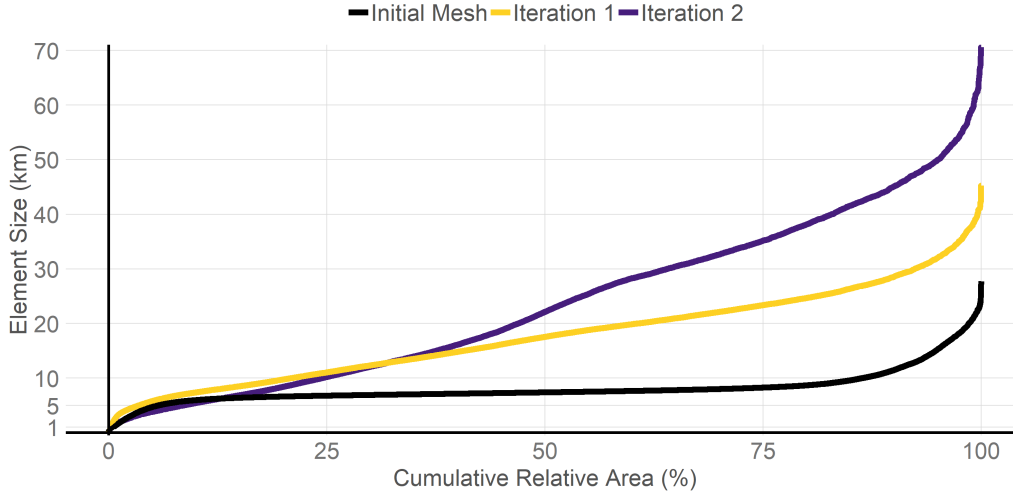


Figure 4: The local element size (km) related to the cumulative relative area (%) that encompasses the western North Atlantic model domain.

428 (Figure 5G). The final coastal floodplain mesh contains 557,886 nodes and
 429 1,017,487 elements, which is a 64% reduction in total node count. For the
 430 area shown in Figure 5H, the resolution ranges from 40 - 150 m, with most
 431 of the area containing resolution of 80 - 100 m. The benefits of employing
 432 an unstructured finite element mesh are now better utilized in the new mesh
 433 with the additional benefit of retaining topographic accuracy when compared
 434 to the original source mesh (Figure 5I).

435 The final mesh (coined NGOM-RT), after seaming the new coastal flood-
 436 plain mesh with the inland waterways and LTEA-derived offshore mesh, in-
 437 cludes 2,051,346 nodes and 4,065,583 elements (Figures 6-7). The NGOM-
 438 RT has an overall nodal reduction of 62.7% compared to the high-resolution
 439 NGOM3 mesh. A reduction of 64% in node count spanned element sizes of
 440 less than 100 m, a 53% reduction in nodes sizes between 100 - 200 m, and
 441 a 62% reduction in nodes of element sizes ranging from 200 - 500 m (Figure
 442 8). In addition to coarsening mesh elements in regions of high node density,
 443 such as across the coastal floodplain, mesh node density is coarsened in areas
 444 of open water. The final mesh reduced nodes counts by 77% in element sizes
 445 from 1 - 10 km (Figure 8). Element sizes greater than 10 km now span 75%
 446 of the entire model domain in contrast to the 45% of the original NGOM3
 447 mesh (Figure 9).

448 3.3. Model Validation

449 Hurricanes Ivan, Dennis, Katrina, and Isaac were selected for model vali-
450 dation as they made landfall along the NGOM coast and contain a plethora of
451 measured data. In addition, Bilskie et al. [42] performed a synoptic analysis
452 and detailed validation with an earlier version of the NGOM3 model for all
453 four hurricanes focused on the Mississippi, Alabama, and Florida panhandle.

454 The NGOM3 and NGOM-RT simulated water levels and waves agree
455 with measurements along the Mississippi, Alabama, and Florida panhandle
456 for Hurricanes Ivan, Dennis, Katrina, and Isaac (Tables 1, Figure 10 and
457 Supplementary S1-S8). SI and bias of time-series water levels ranged from
458 0.18 - 0.28 to -0.08 - 0.09 m across the range of storms for the NGOM-RT
459 model simulation, respectively, indicating the simulated time-series water
460 levels agree with the measurements. Simulated peak water levels match
461 measured HWMs (including gage peaks) with estimated peak water level
462 errors ranging from 0.14 - 0.31 m. Combining all HWMs and gage peak
463 errors across the four storms yields a coefficient of determination (R^2) of
464 0.96 for both models and a slope of the linear regression line of 0.95 and 0.98
465 for the NGOM3 and NGOM-RT models, respectively.

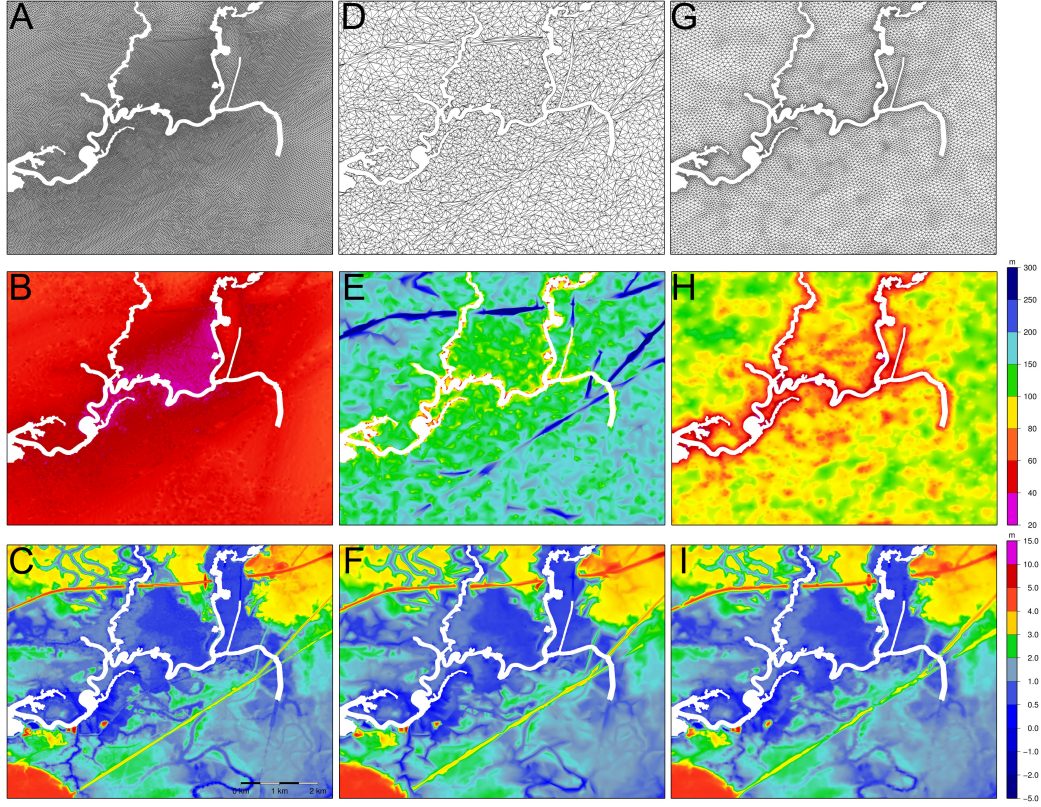


Figure 5: Unstructured finite element mesh across the floodplain near Pascagoula, MS as represented by the A) research-grade mesh (43,336 nodes and 84,756 elements as shown), D) decimated mesh (4,746 nodes and 8,128 elements as shown), and G) real-time-grade mesh (11,976 nodes and 22,051 elements as shown). Local element size (m) and topography (m, NAVD88) as represented by the B-C) research-grade mesh, E-F) decimated mesh, and H-I) real-time-grade mesh, respectively. Water bodies have been removed for visualization and analysis purposes.

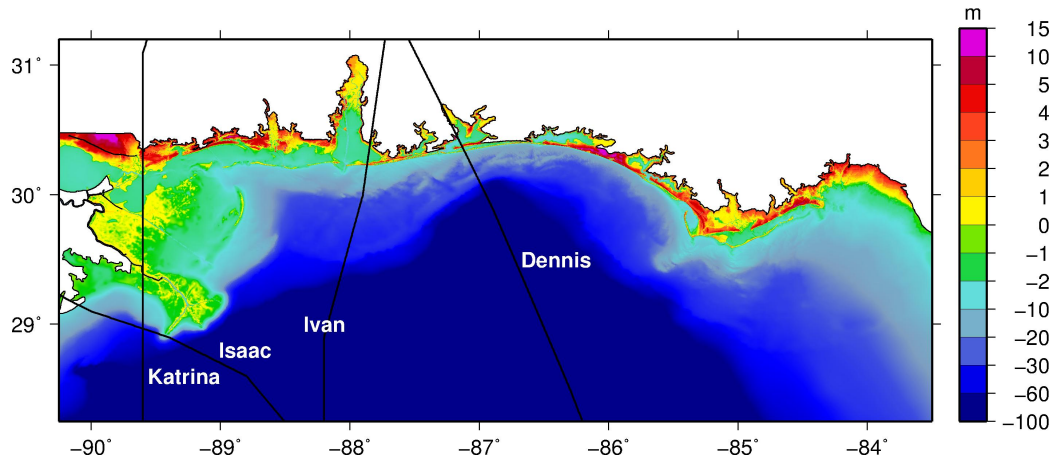


Figure 6: Topography and bathymetry are represented by the NGOM-RT unstructured finite element mesh (m, NAVD88). Hurricane tracks are shown as the black lines.

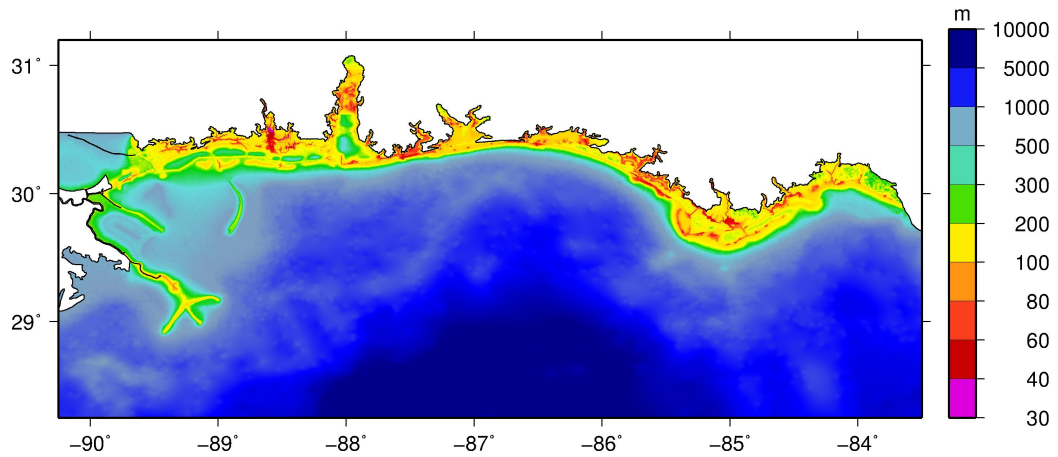


Figure 7: Local element size (m) of the NGOM-RT unstructured finite element mesh.

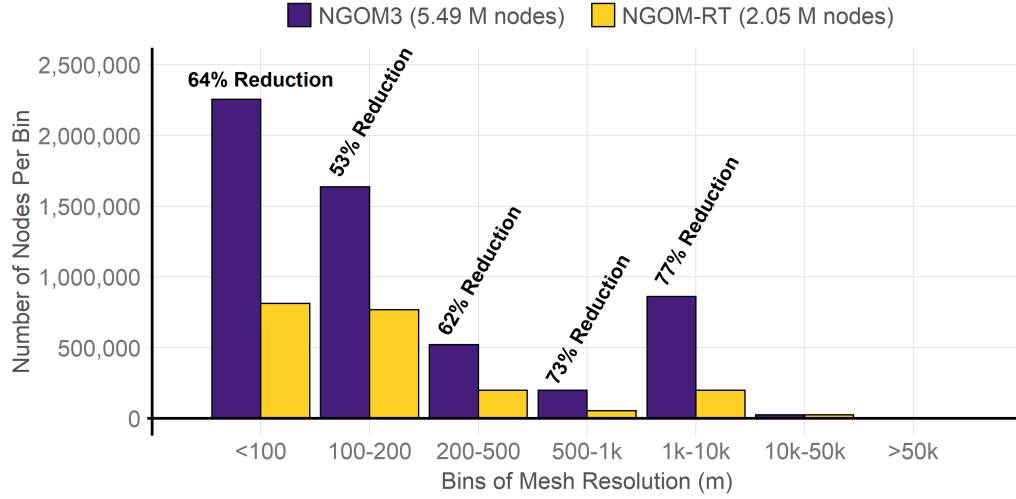


Figure 8: Bins of mesh resolution for the original NGOM3 and final mesh (NGOM-RT).

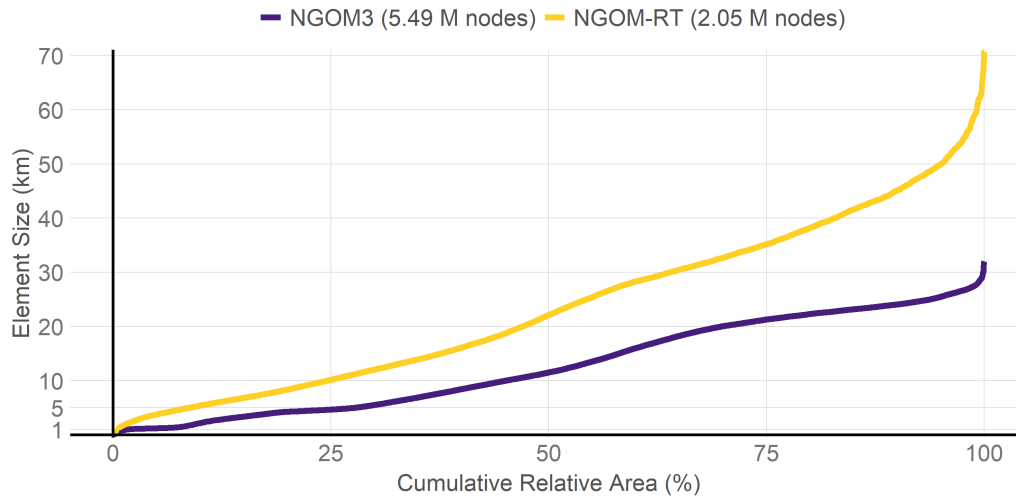


Figure 9: The local element size (km) related to the cumulative relative area (%) that encompasses the western North Atlantic model domain for the initial NGOM3 and final NGOM-RT unstructured meshes.

Table 1: Summary of NGOM-RT water level statistics for recorded water level measurements. SI and bias were only computed for time-series data. Statistics and errors for peak storm surge were only computed if the data set had 10 reliable stations.

Storm	Data Source	No. of stations	ADCIRC to measured HWMs				Measured HWMs				Estimated ADCIRC errors			
			SI (m)	Bias	No. of HWMs	Slope	R^2	Avg.	Abs. Diff. (m)	Std. Dev. (m)	Avg.	Abs. Diff. (m)	Std. Dev. (m)	Std. Dev. (m)
Ivan	NOAA	3	0.213	0.143										
	USACE	8	0.302	0.076										
	FEMA													
Dennis	All	11	0.278	0.094	124	0.87	0.52		0.461	0.527	0.135	0.311	0.228	0.446
	NOAA/NDBC	14	0.242	-0.036	14	0.99	0.98		0.060	0.063	0.135	0.002	0.080	0.446
	FEMA				146	0.91	0.71		0.246	0.263	0.058	0.205	0.080	0.000
Katrina	All	14	0.242	-0.036	158	0.92	0.78		0.224	0.241	0.041	0.180	0.078	0.250
	NOAA	9	0.248	-0.003							0.044			0.228
	USACE	15	0.186	0.001	12	1.02	0.96		0.105	0.146	0.000	0.105	0.000	0.146
Isaac	USGS	6	0.230	-0.060										
	FEMA				314	0.99	0.96		0.298	0.372	0.104	0.195	0.201	0.313
	All	30	0.213	-0.012	326	0.99	0.96		0.291	0.366	0.105	0.187	0.202	0.306
USGS Perm.	NOAA	15	0.188	-0.039	16	1.00	0.94		0.071	0.085	0.000	0.071	0.000	0.085
	USGS SSS	13	0.251	-0.147	12	0.99	0.88		0.191	0.246	0.000	0.191	0.000	0.246
	USGS Rapid	53	0.168	-0.071	42	1.01	0.88		0.124	0.105	0.000	0.124	0.000	0.105
NOAA HWM	USGS Rapid	7	0.167	-0.102										
	NOAA HWM	88	0.184	-0.079	42	0.98	0.70		0.286	0.337	0.067	0.219	0.129	0.311
	All				112	0.98	0.88		0.177	0.215	0.042	0.136	0.087	0.197

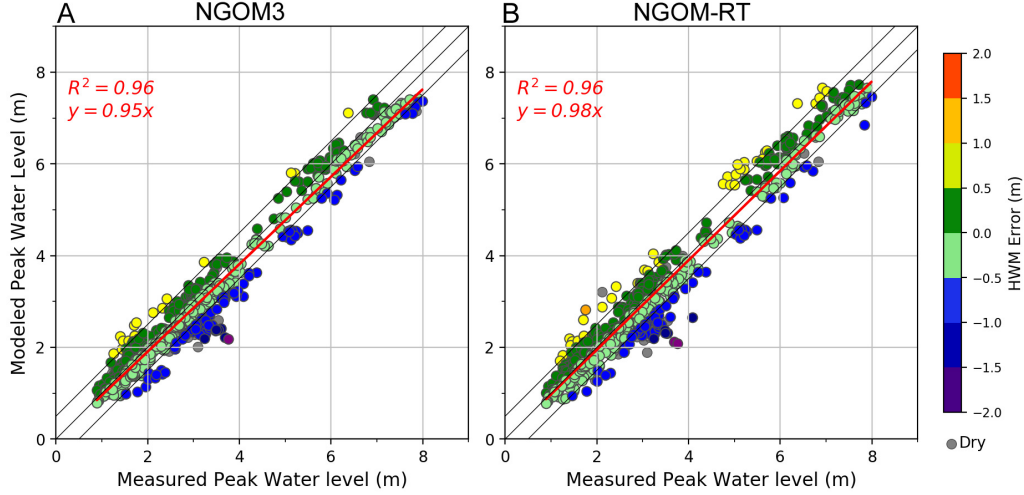


Figure 10: Comparison of measured and simulated peak surges (high water marks and gage peaks) for Hurricanes Ivan (2004), Dennis (2005), Katrina (2005), and Isaac (2012) for the A) NGOM3 and B) NGOM-RT models.

3.4. NGOM3 and NGOM-RT Intercomparison

Table 2 shows difference among the error statistics between the NGOM3 and NGOM-RT model results. Similar to the minor differences in the HWM errors (Figure 10) there is virtually no difference in the error statistics. Differences in SI and bias are less than 10 cm. The differences between the model's errors (with respect to the average absolute difference) range from -0.04 - 0.02 m. These results can be considered negligible. Larger differences in model errors are found for Hurricanes Katrina and Isaac, albeit they are still minor. These storms made landfall along the Louisiana/Mississippi border and differences are a result of the addition of flood protection infrastructure in southeastern Louisiana in the NGOM-RT mesh.

To this point, simulated water levels have been compared to measurements and errors were similar among the NGOM3 and NGOM-RT models. To compare simulated water levels between the NGOM3 and NGOM-RT models across the full coastal floodplain RMS differences (Eq. 6) were calculated for mesh nodes shallower than 10 m [77] (including normally dry areas) in the region surrounding the landfall location. For comparison purposes, the NGOM-RT results were linearly interpolated to the NGOM3 mesh. The RMS difference in simulated peaks was 0.11 m, 0.10 m, 0.18 m, and 0.55

Table 2: Summary of differences in water level error statistics between the NGOM3 and NGOM-RT model results (NGOM3 - NGOM-RT). SI and bias were only computed for time-series data. Statistics and errors for peak storm surge were only computed if the data set had 10 reliable stations.

Storm	Data Source	No. of stations	ADCIRC to measured HWMs					Estimated ADCIRC errors	
			SI (m)	Bias	No. of HWMs	Slope	R^2	Avg. Abs. Diff. (m)	Std. Dev. (m)
Ivan	NOAA	3	0.01	0.06					
	USACE	8	-0.02	-0.01					
	FEMA				126	-0.01	-0.06	0.02	0.00
Dennis	All	11	-0.01	0.01	126	-0.01	-0.06	0.02	0.00
	NOAA/NDBC	14	-0.01	0.00	14	0.00	-0.01	0.02	0.03
	FEMA				148	0.00	-0.02	0.01	0.01
Katrina	All	14	-0.01	0.00	162	-0.01	-0.04	0.01	0.02
	NOAA	9	-0.02	-0.01					
	USACE	16	-0.01	0.00	12	-0.01	-0.03	-0.02	-0.05
Isaac	USGS	7	-0.03	-0.02					
	FEMA				311	-0.02	0.01	-0.01	-0.06
	All	32	-0.02	-0.01	323	-0.02	0.01	-0.01	-0.05
	NOAA	16	0.08	0.08	16	-0.03	0.01	0.00	0.01
	USGS Perm.	13	0.03	0.05	12	-0.04	0.06	-0.04	-0.10
	USGS SSS	59	0.03	0.00	42	-0.05	0.03	0.04	0.07
	USGS Rapid	7	0.05	0.01					
	NOAA HWM				42	-0.05	0.02	-0.03	-0.07
	All	95	0.04	0.02	112	-0.04	0.01	-0.01	-0.03

485 m for Hurricanes Ivan, Dennis, Katrina, and Isaac, respectively. The RMS
486 differences are larger for Katrina and Isaac because these storms impacted
487 western Mississippi and southeastern Louisiana and the addition of the flood
488 protection infrastructure in the NGOM-RT model has an effect on the sim-
489 ulated water levels.

490 4. Benchmarking

491 4.1. High Performance Computing Cluster

492 The NGOM3 and NGOM-RT ADCIRC+SWAN models were bench-
493 marked on two high-performance computing (HPC) systems, Queenbee2 and
494 Stampede2. These HPC systems were selected as they are employed during
495 a real-time hurricane event with the ADCIRC Prediction System (APS).
496 Model benchmarking was performed in order to determine the reduced com-
497 putational cost of the NGOM-RT model as well as the expected wall-clock
498 time.

499 Queenbee2 (<http://www.hpc.lsu.edu>) is a located in Baton Rouge,
500 Louisiana and is maintained by the Louisiana Optical Network Infrastructure
501 (LONI). It consists of 480 compute nodes of two 10-core 2.8 GHz E5-2680v2
502 Xeon processors and 64 GB memory shared across each compute node. The

503 computed nodes are connected via 56 Gb/sec FDR Infiniband. The theoret-
504 ical peak performance of Queenbee2 is 1.5 Petaflops.

505 Stampede2 (<https://portal.tacc.utexas.edu/user-guides/stampede2>) is lo-
506 cated in Austin, Texas and is maintained by the Texas Advanced Computing
507 Center (TACC). It consists of 4,200 KNL and 1,736 SKX compute nodes. For
508 this study, the SKX compute nodes are exclusively used. The SKX compute
509 nodes contain Intel Xeon Platinum 8160 ("Skylake") processors with 48 cores
510 on two sockets (24 cores/socket) and nominal clock rate of 2.1 GHz (1.4-3.7
511 GHz depending on instruction set and number of active cores). Each com-
512 pute node shares 192 GB of RAM. The compute nodes are connected via a
513 100Gb/sec Intel Omni-Path network.

514 4.2. Benchmarking Results

515 The following benchmarking results are presented to connect the reduc-
516 tion in mesh node count to a reduction in wall clock time using the ADCIRC
517 and ADCIRC+SWAN codes. In addition, the results are aimed at high-
518 lighting the expected wall clock when running the NGOM3 and NGOM-RT
519 meshes in real-time. The results presented herein are not focused on tim-
520 ing of the ADCIRC and ADCIRC+SWAN codes or to compare speeds of
521 Stampede2 and Queenbee2.

522 The NGOM3 and NGOM-RT meshes were run with both ADCIRC
523 and ADCIRC+SWAN for Hurricane Katrina. Each run was hot-started at
524 2005/08/28/0000Z and run for two days until 2005/08/30/0000Z which cap-
525 tures the the peak storm surge along the Mississippi coast. This is similar
526 to benchmarking performed by Dietrich et al. [10] for an ADCIRC+SWAN
527 model of southeastern Louisiana. The generalized asymmetrical Holland vor-
528 tex model (GAHM) ([78, 79, 77]) was used as the meteorological forcing for
529 all benchmarking simulations - it is the wind model currently used during
530 real-time simulations. Model output was turned off for all runs. The total
531 wall clock for the two-day simulation was normalized to yield wall clock time
532 per day of simulation.

533 Figure 11 shows the wall clock time as a function of the total number
534 of compute cores and Figure 12 shows the wall clock as a function of the
535 number of mesh nodes per core. The black lines represent the timing of
536 the NGOM3 mesh and the gray represents the NGOM-RT mesh. The circle
537 symbols correspond with an ADCIRC only simulation and diamond with
538 an ADCIRC+SWAN simulation. The shaded region in Figures 11 and 12

539 represent the ideal wall clock (or turn-around time) of 1-2 hours for a five-
540 day forecast simulation.

541 First, we note that the NGOM3 ADCIRC and ADCIRC+SWAN simula-
542 tions scale linearly to 5,760 cores on Stampede2. However, the NGOM-RT
543 ADCIRC and ADCIRC+SWAN simulations scale linearly to 3,840 cores. On
544 Queenbee2 the NGOM3 ADCIRC simulations scale until 1,040 cores and AD-
545 CIRC+SWAN through 3,840 cores (the maximum number of cores we were
546 able to employ on Queenbee2). The NGOM-RT ADCIRC simulation scales
547 linearly until 1,040 cores and 1,920 cores with ADCIRC+SWAN.

548 The timing information indicates that the NGOM-RT mesh on Stam-
549 pede2 can complete a five-day ADCIRC and ADCIRC+SWAN forecast sim-
550 ulation in under two hours using 240 and 960 cores, respectively, compared
551 to 480 and 1,040 cores with the NGOM3. On Queenbee2, a five-day simu-
552 lation can complete in less than two hours using 960 and 1,440 cores on the
553 NGOM-RT mesh using ADCIRC and ADCIRC+SWAN, respectively, and
554 1,040 and 2,880 cores with the NGOM3 mesh.

555 Second, we find that the NGOM-RT mesh reaches its scaling limit earlier
556 than NGOM3. The wall clock converges and reaches a lower limit of 270 sec-
557 onds at 4,800 cores for the NGOM3 and NGOM-RT ADCIRC simulation on
558 Stampede2. The convergence also corresponds to a lower limit of 1,000 nodes
559 per computational core. The SWAN+ADCIRC simulations on Stampede2
560 converge at 7,680 cores with a wall clock lower limit of 600 seconds, which
561 corresponds to a lower limit of 700 mesh nodes per core. The reduced scaling
562 limit of NGOM-RT is related to the reduced mesh node count. The lower
563 limit of mesh nodes per core is achieved faster with the NGOM-RT mesh.
564 The increased parallel communication becomes the limiting factor when the
565 total number of mesh nodes per computational core is reduced (total number
566 of computational cores is increased).

567 Furthermore, there is negligible performance decrease in deploying greater
568 than 4,800 and 7,680 Stampede2 cores for an NGOM-RT ADCIRC and AD-
569 CIRC+SWAN simulation, respectively. In addition, there is no gain in wall
570 clock time when decomposing the unstructured mesh to less than 1,000 nodes
571 per computational core for an ADCIRC simulation and 700 mesh nodes per
572 core for an ADCIRC+SWAN simulation for either mesh. On Queenbee2
573 there is a benefit in utilizing up to 3,840 cores and decomposing the mesh
574 into 1,400 nodes per core with NGOM3 and 500 nodes per core with NGOM-
575 RT for both an ADCIRC and ADCIRC+SWAN simulation.

576 To complete a five-day simulation on Stampede2 in under two hours the

577 NGOM3 mesh requires a maximum of 10,000 and 4,000 mesh nodes per core
 578 for ADCIRC and ADCIRC+SWAN, respectively. The NGOM-RT mesh re-
 579 quires a maximum of 20,000 and 6,000 mesh nodes per core for for AD-
 580 CIRC and ADCIRC+SWAN, respectively. On Queenbee2 an ADCIRC and
 581 ADCIRC+SWAN simulation requires a maximum of 9,000 and 2,000 mesh
 582 nodes per core, respectively, and 10,000 and 3,000 mesh nodes per on the
 583 NGOM-RT mesh.

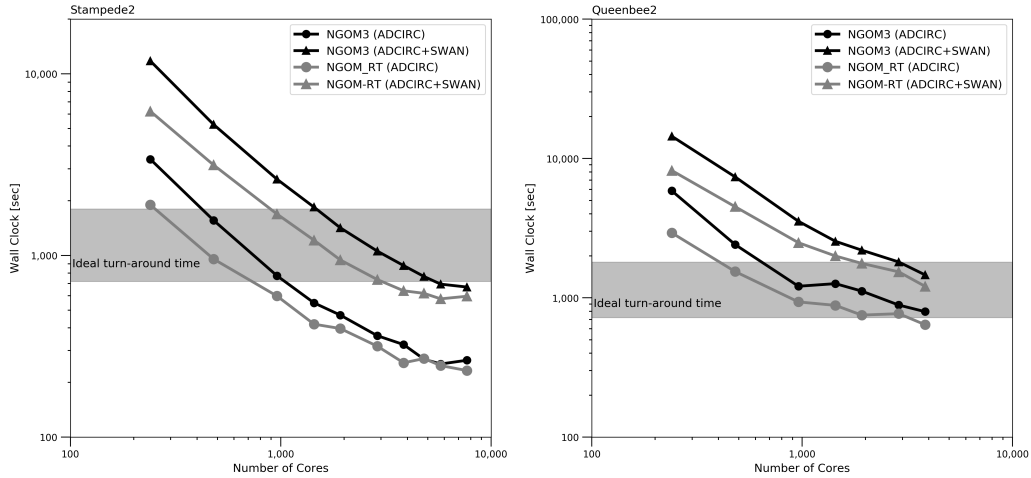


Figure 11: Wall-clock time (seconds) versus total number of computational cores for the NGOM3 (black) and NGOM-RT (gray) models on Stampede2 (left) and Queenbee2 (right). The shaded region represents the ideal wall clock time to complete a five-day forecast simulation within 1-2 hours.

584 Finally, we quantify the reduction in wall clock for the NGOM-RT mesh
 585 relative to the NGOM3 mesh as shown in Figure 13. On 240 cores the
 586 NGOM-RT mesh is 1.8-2.0 times faster than NGOM3 for ADCIRC and
 587 ADCIRC+SWAN on Stampede2 and Queenbee2. On Stampede2, the AD-
 588 CIRC+SWAN simulation benefits when using larger core counts than AD-
 589 CIRC only simulations. There is a spike of 1.25 in the normalized speed-up
 590 at 3,840 cores on Stampede2 and 1.5 from 1,440 - 1,920 cores on Queenbee2
 591 for the ADCIRC simulation.

592 5. Conclusions

593 Accurate numerical simulation of astronomic tide- and tropical cyclone-
 594 driven water level anomalies are dependent on the underlying unstructured

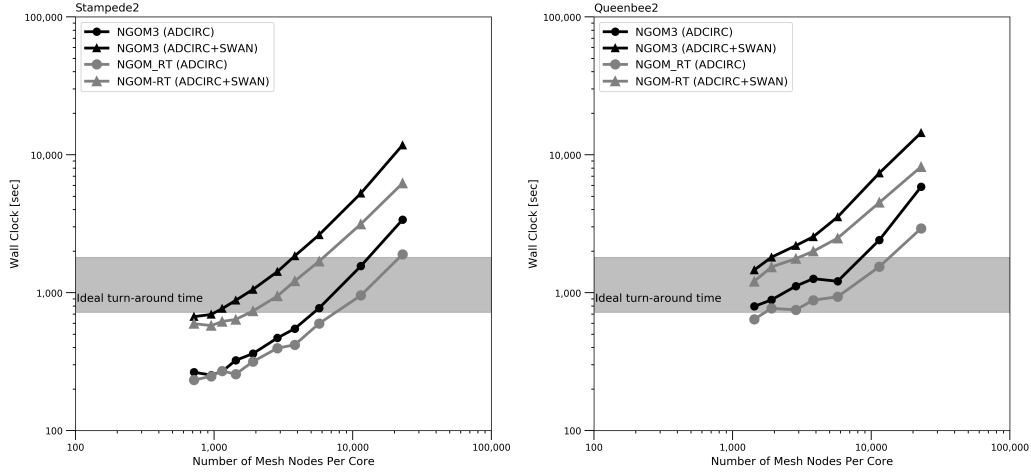


Figure 12: Wall-clock time (seconds) versus unstructured mesh nodes per core for the NGOM3 (black) and NGOM-RT (gray) models on Stampede2 (left) and Queenbee2 (right). The shaded region represents the ideal wall clock time to complete a five-day forecast simulation within 1-2 hours.

595 mesh and its representation of the natural landscape. Computational hur-
 596 ricane storm surge models are now used to in decision support frameworks
 597 during an impending tropical cyclone event to protect lives and property.
 598 Therefore, it is imperative that an accurate simulation be performed with a
 599 fast turnaround time (1-2 hours). In addition, the model must include suffi-
 600 cient detail across the coastal floodplain so guidance can be provided beyond
 601 the shoreline where property and infrastructure exist.

602 Previously developed unstructured mesh generation methods for shallow
 603 water equation models, such as LTEA and LTEA+CD, are able to gener-
 604 ate computationally efficient unstructured meshes for the deep water and
 605 nearshore areas (always wetted). However, there is a gap in such research
 606 for computationally efficient mesh generation across the coastal floodplain.
 607 This work begins to address this gap while building on previous efforts in
 608 order to construct a high-quality unstructured mesh for use in a real-time
 609 early-warning hurricane storm surge guidance system.

610 We utilized a mesh decimation algorithm for the coastal floodplain with
 611 the goal of reducing mesh nodes while preserving the representation of the
 612 topography. An unstructured mesh was generated via paving scalar density
 613 from the obtained size functions along with interior vertical feature con-
 614 straints and the external model boundary. The resulting mesh, real-time

615 mesh, contains 64% less computational points than the research-grade mesh
 616 and preserved the integrity of the meshes representation of the coastal topog-
 617 raphy. Simulated water levels for both models agree with measurements for
 618 Hurricanes Ivan, Dennis, Katrina, and Isaac. Differences in SI and bias for
 619 time-series water levels were less than 10 cm and differences in average abso-
 620 lute difference range from -0.04 - 0.02 m. In addition, an ADCIRC+SWAN
 621 simulation with the NGOM-RT mesh is 1.5-2.0 times faster than the NGOM3
 622 mesh on up to 1,920 cores on Stampede2 and 960 cores on Queenbee2. The
 623 NGOM-RT mesh requires 480 and 960 less cores to perform a five-day AD-
 624 CIRC+SWAN simulation in under 2 hours on Stampede2 and Queenbee2,
 625 respectively.

626 Future work will improve mesh generation across the coastal floodplain
 627 with focus on generating computationally efficient meshes. New methods
 628 will supplement geometric mesh generation approaches to integrate shallow
 629 water hydrodynamics into the mesh generation procedure. The next gen-
 630 eration of unstructured mesh generation techniques will be fully-automated
 631 and be based on a high-resolution digital elevation models. As computational
 632 power continues to increase storm surge forecasting models that provide early
 633 warning can increase in their domain size and include higher resolution while
 634 continuing to reduce the computational cost.

635 **Acknowledgements**

636 This research was funded in part under the U.S. Department of Homeland
 637 Security [Award No. 2015-ST-061-ND0001-01], the National Oceanic and
 638 Atmospheric Administration (NOAA) Ecological Effects of Sea Level Rise
 639 (EESLR) Program [Award Nos. NA10NOS4780146 and NA16NOS4780208],
 640 and the Louisiana Sea Grant Laborde Chair. This work used the Extreme
 641 Science and Engineering Discovery Environment (XSEDE), which is sup-
 642 ported by the National Science Foundation (NSF) [Award No. ACI-1053575]
 643 [80]. This work also used High Performance Computing at Louisiana State
 644 University (LSU) and the Louisiana Optical Network Initiative (LONI). The
 645 statements and conclusions are those of the authors and do not necessar-
 646 ily reflect the views of NOAA, Louisiana Sea Grant, XSEDE, NSF, LSU, or
 647 LONI. All data for this paper is properly cited and referred to in the reference
 648 list.

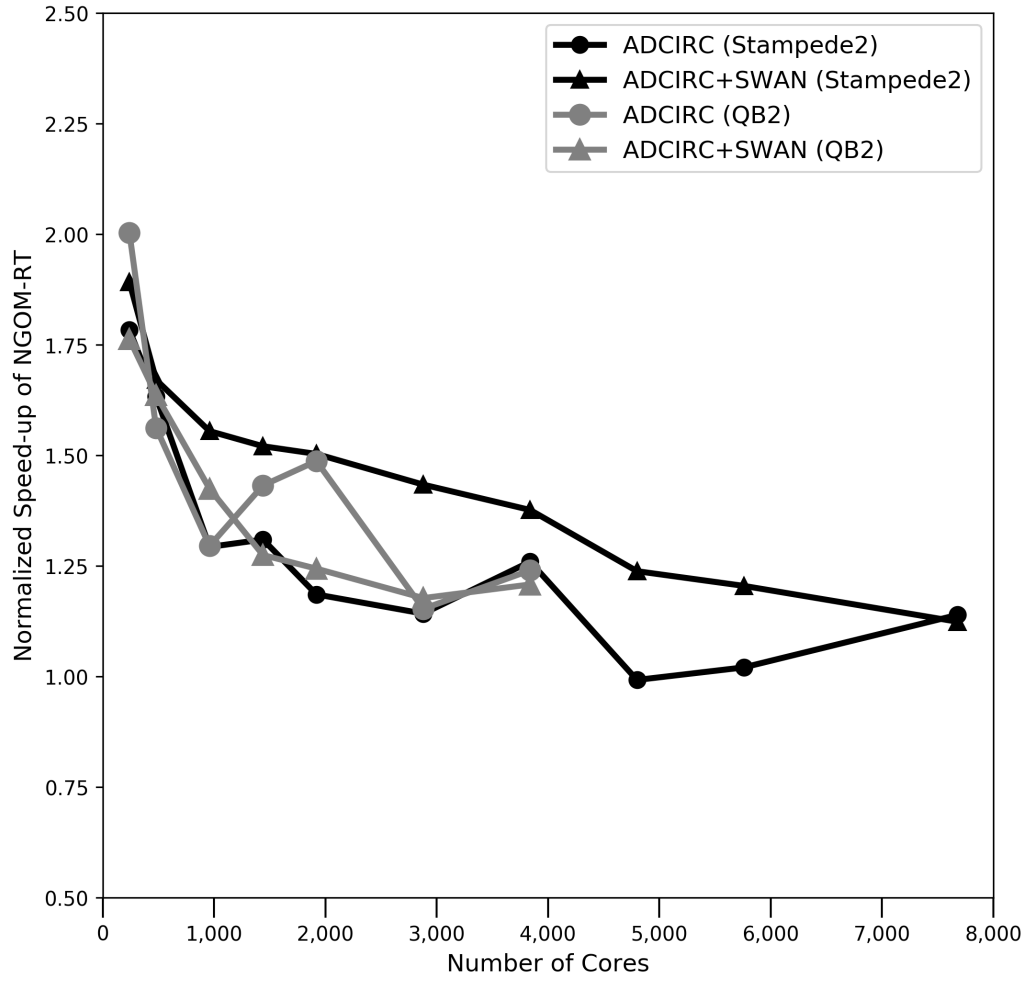


Figure 13: Normalized speed-up of the NGOM-RT model as a function of total number of cores on Stampede2 (black) and Queenbee2 (gray). The NGOM-RT runs are normalized by the NGOM runs for the same number of cores.

649 References

- 650 [1] S. T. Ashley, W. S. Ashley, Flood fatalities in the united states, *Journal*
651 *of Applied Meteorology and Climatology* 47 (2008) 805–818.
- 652 [2] R. Munroe, B. Montz, S. Curtis, Getting more out of storm surge
653 forecasts: Emergency support personnel needs in north carolina, *Wea.*
654 *Climate Soc.* 10 (2018) 813–820.
- 655 [3] B. Wolshon, E. Urbina, C. Wilmot, M. Levitan, Review of policies
656 and practices for hurricane evacuation. i: Transportation planning, pre-
657 paredness, and response 6 (2005) 129–142.
- 658 [4] M. V. Bilskie, D. Coggin, S. C. Hagen, S. C. Medeiros, Terrain-driven
659 unstructured mesh development through semi-automatic vertical feature
660 extraction, *Advances in Water Resources* 86, Part A (2015) 102–118.
- 661 [5] M. Bilskie, S. C. Hagen, Topographic accuracy assessment of bare earth
662 lidar-derived unstructured meshes, *Advances in Water Resources* 52
663 (2013) 165–177.
- 664 [6] Z. Cobell, H. Zhao, H. J. Roberts, F. R. Clark, S. Zou, Surge and wave
665 modeling for the louisiana 2012 coastal master plan, *Journal of Coastal*
666 *Research* (2013) 88–108.
- 667 [7] M. Hope, J. Westerink, A. Kennedy, P. Kerr, J. Dietrich, C. Dawson,
668 C. Bender, J. Smith, R. Jensen, M. Zijlema, L. Holthuijsen, R. Luettich,
669 M. Powell, V. Cardone, A. Cox, H. Pourtaheri, H. Roberts, J. Atkinson,
670 S. Tanaka, H. Westerink, L. Westerink, Hindcast and validation of
671 hurricane ike (2008) waves, forerunner, and storm surge, *Journal of*
672 *Geophysical Research: Oceans* (2013).
- 673 [8] S. Medeiros, S. Hagen, J. Weishampel, J. Angelo, Adjusting lidar-
674 derived digital terrain models in coastal marshes based on estimated
675 aboveground biomass density, *Remote Sensing* 7 (2015) 3507.
- 676 [9] S. Bunya, J. Dietrich, J. Westerink, B. Ebersole, J. Smith, J. Atkinson,
677 R. Jensen, D. Resio, R. Luettich, C. Dawsons, V. Cardone, A. Cox,
678 M. Powell, H. Westerink, H. Roberts, A high-resolution coupled riverine
679 flow, tide, wind, wind wave, and storm surge model for southeastern

- 680 louisiana and mississippi. part i: Model development and validation,
681 Monthly Weather Review 128 (2010).
- 682 [10] J. Dietrich, S. Tanaka, J. Westerink, C. Dawson, R. Luettich, M. Zijlema, L. Holthuijsen, J. Smith, L. Westerink, H. Westerink, Performance of the unstructured-mesh, swan+adcirc model in computing hurricane waves and surge, Journal of Scientific Computing 52 (2012) 468–497.
683
684
685
686
- 687 [11] J. Dietrich, J. Westerink, A. Kennedy, J. Smith, R. Jensen, M. Zijlema, L. Holthuijsen, C. Dawson, R. Luettich, M. Powell, V. Cardone, A. Cox, G. Stone, H. Pourtaheri, M. Hope, S. Tanaka, L. Westerink, H. Westerink, Z. Cobell, Hurricane gustav (2008) waves and storm surge: Hindcast, synoptic analysis, and validation in southern louisiana, Monthly Weather Review 139 (2011) 2488–2522.
688
689
690
691
692
- 693 [12] J. Dietrich, M. Zijlema, J. Westerink, L. Holthuijsen, C. Dawson, R. Luettich, R. Jensen, J. Smith, G. Stelling, G. Stone, Modeling hurricane waves and storm surge using integrally-coupled, scalable computations, Coastal Engineering 58 (2011) 45–65.
694
695
696
- 697 [13] J. Dietrich, M. Zijlema, P. E. Allier, L. Holthuijsen, N. Booij, J. D. Meixner, J. K. Proft, C. N. Dawson, C. J. Bender, A. Naimaster, J. M. Smith, J. J. Westerink, Limiters for spectral propagation velocities in swan, Ocean Modelling 70 (2013) 85–102.
698
699
700
- 701 [14] Y. Funakoshi, S. C. Hagen, P. Bacopoulos, Coupling of hydrodynamic and wave models: Case study for hurricane floyd (1999) hindcast, Journal of Waterway, Port, Coastal, and Ocean Engineering 134 (2008).
702
703
- 704 [15] P. G. Black, E. A. D’Asaro, T. B. Sanford, W. M. Drennan, J. A. Zhang, J. R. French, P. P. Niiler, E. J. Terrill, E. J. Walsh, Airsea exchange in hurricanes: Synthesis of observations from the coupled boundary layer airsea transfer experiment, Bulletin of the American Meteorological Society 88 (2007) 357–374.
705
706
707
708
- 709 [16] M. D. Powell, P. J. Vickery, T. A. Reinhold, Reduced drag coefficient for high wind speeds in tropical cyclones, Nature 422 (2003) 279–283.
710

- 711 [17] M. Powell, Drag coefficient distribution and wind speed dependence in
712 tropical cyclones, Report, Atlantic Oceanographic and Meteorological
713 Laboratory, 2006.
- 714 [18] B. H. Morrow, J. K. Lazo, Coastal emergency managers' preferences for
715 storm surge forecast communication, *J Emerg Manag* 12 (2014) 153–60.
- 716 [19] J. Burston, D. Ware, R. Tomlinson, The real-time needs of emergency
717 managers for tropical cyclone storm tide forecasting: results of a par-
718 ticipatory stakeholder engagement process, *Natural Hazards* 78 (2015)
719 1653–1668.
- 720 [20] G. J. Gorman, M. D. Piggott, M. R. Wells, C. C. Pain, P. A. Alli-
721 son, A systematic approach to unstructured mesh generation for ocean
722 modelling using *gmt* and *terreno*, *Computers Geosciences* 34 (2008)
723 1721–1731.
- 724 [21] A. Bilgili, K. W. Smith, D. R. Lynch, Battri: A two-dimensional
725 bathymetry-based unstructured triangular grid generator for finite ele-
726 ment circulation modeling, *Computers Geosciences* 32 (2006) 632–642.
- 727 [22] S. Danilov, Ocean modeling on unstructured meshes, *Ocean Modelling*
728 69 (2013) 195–210.
- 729 [23] S. C. Hagen, J. J. Westerink, R. L. Kolar, O. Horstmann, Two-
730 dimensional, unstructured mesh generation for tidal models, *Interna-
731 tional Journal for Numerical Methods in Fluids* 35 (2001) 669–686.
- 732 [24] J. J. WESTERINK, R. A. LUETTICH JR., J. C. MUCCINO, Mod-
733 elling tides in the western north atlantic using unstructured graded grids,
734 *Tellus A* 46 (1994) 178–199.
- 735 [25] S. C. Hagen, O. Horstmann, R. J. Bennett, An unstructured mesh
736 generation algorithm for shallow water modeling, *International Journal
737 of Computational Fluid Dynamics* 16 (2002) 83–91.
- 738 [26] S. Hagen, A. Zundel, S. Kojima, Automatic, unstructured mesh gener-
739 ation for tidal calculations in a large domain, *International Journal of
740 Computational Fluid Dynamics* 20 (2006) 593–608.

- 741 [27] D. M. Parrish, S. C. Hagen, 2d unstructured mesh generation for oceanic
742 and coastal tidal models from a localized truncation error analysis with
743 complex derivatives, *International Journal of Computational Fluid Dy-*
744 *namics* 21 (2007) 277–296.
- 745 [28] D. M. Parrish, S. C. Hagen, Incorporating spatially variable bottom
746 stress and coriolis force into 2d, a posteriori, unstructured mesh gen-
747 eration for shallow water models, *International Journal for Numerical*
748 *Methods in Fluids* 60 (2009) 237–261.
- 749 [29] P. Bacopoulos, D. Parrish, S. Hagen, Unstructured mesh assessment
750 for tidal model of the south atlantic bight and its estuaries, *Journal of*
751 *Hydraulic Engineering, Special Issue on Coastal Maritime Hydraulics* 49
752 (2011) 487–502.
- 753 [30] P.-O. Persson, G. Strang, A simple mesh generator in matlab, *SIAM*
754 *Review* 46 (2004) 329–345.
- 755 [31] C. Conroy, E. Kubatko, D. West, Admesh:an advanced, automatic un-
756 structured mesh generator for shallow water models, *Ocean Dynamics*
757 62 (2012) 1503–1517.
- 758 [32] K. J. Roberts, W. J. Pringle, J. J. Westerink, Oceanmesh2d 1.0: Matlab-
759 based software for two-dimensional unstructured mesh generation in
760 coastal ocean modeling, *Geosci. Model Dev. Discuss.* 2018 (2018) 1–
761 36.
- 762 [33] S. Medeiros, S. Hagen, J. Weishampel, Comparison of floodplain surface
763 roughness parameters derived from land cover data and field measure-
764 ments, *Journal of Hydrology* 452453 (2012) 139–149.
- 765 [34] S. Medeiros, S. C. Hagen, Review of wetting and drying algorithms
766 for numerical tidal flow models, *International Journal for Numerical*
767 *Methods in Fluids* 71 (2012) 473–487.
- 768 [35] D. Coggin, S. Hagen, M. B. Salisbury, A digital elevation model for
769 franklin, wakulla, and jefferson counties, *Florida Watershed Journal* 4
770 (2011) 5–10.
- 771 [36] I. Kinnmark, The shallow water wave equations: formulation, analysis,
772 and application, Springer-Verlag, New York, New York.

- 773 [37] R. Kolar, W. Gray, J. Westerink, M. Cantekin, C. Blain, Aspects of
774 nonlinear simulations using shallow-water models based on the wave
775 continuity equation, *Computers and Fluids* 23 (1994) 523–538.
- 776 [38] R. Luettich, J. Westerink, Formulation and numerical implementations
777 of the 2D/3D ADCIRC finite element model version 44.XX, Report,
778 12/08/2004, 2004.
- 779 [39] J. Westerink, R. Luettich, J. Feyen, J. Atkinson, C. Dawson, H. Roberts,
780 M. Powell, J. Dunion, E. Kubatko, H. Pourtaheri, A basin- to channel-
781 scale unstructured grid hurricane storm surge model applied to southern
782 lousiana, *Monthly Weather Review* 136 (2008) 833–864.
- 783 [40] J. Atkinson, H. Roberts, S. Hagen, S. Zou, P. Bacopoulos, S. C.
784 Medeiros, J. Weishampel, Z. Cobell, Deriving frictional parameters and
785 performing historical validation for an adcirc storm surge model of the
786 florida gulf coast, *Florida Watershed Journal* 4 (2011) 22–27.
- 787 [41] B. Buczkowski, J. Reid, J. Jenkins, C. Reid, S. Williams, J. Flocks,
788 usSEABED: Gulf of Mexico and Caribbean (Puerto Rico and U.S. Vi-
789 rigin Islands) offshore surficial sediment data release, Report, U.S. Ge-
790 ological Survey, 2006.
- 791 [42] M. V. Bilskie, S. C. Hagen, S. C. Medeiros, A. T. Cox, M. Salisbury,
792 D. Coggin, Data and numerical analysis of astronomic tides, wind-waves,
793 and hurricane storm surge along the northern gulf of mexico, *Journal*
794 *of Geophysical Research: Oceans* 121 (2016) 3625–3658.
- 795 [43] A. Kennedy, U. Gravois, B. Zachry, J. Westerink, M. Hope, R. Luettich,
796 R. G. Dean, Origin of the hurricane ike forerunner surge, *Geophysical*
797 *Research Letters* 38 (2011).
- 798 [44] R. Martyr, J. Dietrich, J. Westerink, P. Kerr, C. Dawson, J. Smith,
799 H. Pourtaheri, M. Powell, M. Van Ledden, S. Tanaka, H. J. Roberts,
800 H. Westerink, L. Westerink, Simulating hurricane storm surge in the
801 lower mississippi river under varying flow conditions, *Journal of Hy-*
802 *draulic Engineering* 139 (2013) 492–501.
- 803 [45] N. Booij, R. Ris, L. Holthuijsen, A third-generation wave model for
804 coastal regions 1. model description and validation, *Journal of Geo-*
805 *physical Research* 104 (1999) 7649–7666.

- 806 [46] R. Ris, L. Holthuijsen, N. Booij, A third-generation wave model for
807 coastal regions 2. verification, *Journal of Geophysical Research* 104
808 (1999) 7667–7681.
- 809 [47] M. Zijlema, Computation of wind-wave spectra in coastal waters with
810 swan on unstructured grids, *Coastal Engineering* 57 (2010) 267–277.
- 811 [48] L. Cavaleri, P. Rizzoli, Wind wave prediction in shallow water: Theory
812 and applications, *Journal of Geophysical Research: Oceans* 86 (1981)
813 10961–10973.
- 814 [49] G. J. Komen, K. Hasselmann, K. Hasselmann, On the existence of a
815 fully developed wind-sea spectrum, *Journal of Physical Oceanography*
816 14 (1984) 1271–1285.
- 817 [50] W. Rogers, P. Hwang, D. Wang, Investigation of wave growth and
818 decay in the swan model: Three regional-scale applications*, *Journal of*
819 *Physical Oceanography* 33 (2003) 366–389.
- 820 [51] O. Madsen, Y. Poon, H. Graber, Spectral wave attenuation by bottom
821 friction: Theory, *Coastal Engineering Proceedings* (1988) 492–504.
- 822 [52] J. A. Battjes, J. P. F. M. Janssen, Energy loss and set-up due to break-
823 ing of random waves, *Coastal Engineering Proceedings; No 16* (1978):
824 *Proceedings of 16th Conference on Coastal Engineering, Hamburg, Ger-*
825 *many, 1978.* (1978).
- 826 [53] M. Bilskie, S. Hagen, S. C. Medeiros, D. Passeri, Dynamics of sea level
827 rise and coastal flooding on a changing landscape, *Geophysical Research*
828 *Letters* 41 (2014) 927–934.
- 829 [54] M. V. Bilskie, S. C. Hagen, K. Alizad, S. C. Medeiros, D. L. Passeri,
830 H. F. Needham, A. Cox, Dynamic simulation and numerical analysis of
831 hurricane storm surge under sea level rise with geomorphologic changes
832 along the northern gulf of mexico, *Earth’s Future* 4 (2016) 177–193.
- 833 [55] S. C. Hagen, D. Parrish, Meshing requirements for tidal modeling in the
834 western north atlantic, *International Journal of Computational Fluid*
835 *Dynamics* 18 (2004) 585–595.

- 836 [56] S. Hagen, Estimation of the truncation error for the linearized, shallow
837 water momentum equations, *Engineering with Computers* 17 (2001)
838 354–362.
- 839 [57] D. Passeri, S. Hagen, M. Bilskie, S. Medeiros, On the significance of
840 incorporating shoreline changes for evaluating coastal hydrodynamics
841 under sea level rise scenarios, *Natural Hazards* 75 (2015) 1599–1617.
- 842 [58] D. L. Passeri, S. C. Hagen, S. C. Medeiros, M. V. Bilskie, Impacts
843 of historic morphology and sea level rise on tidal hydrodynamics in a
844 microtidal estuary (grand bay, mississippi), *Continental Shelf Research*
845 (2015) CSR3698.
- 846 [59] D. L. Passeri, S. C. Hagen, N. G. Plant, M. V. Bilskie, S. C. Medeiros,
847 K. Alizad, Tidal hydrodynamics under future sea level rise and coastal
848 morphology in the northern gulf of mexico, *Earth’s Future* 4 (2016)
849 159–176.
- 850 [60] M. B. Salisbury, S. C. Hagen, D. Coggin, P. Bacopoulos, J. Atkinson,
851 H. J. Roberts, Unstructured mesh development for the big bend region
852 (florida), *Florida Watershed Journal* 4 (2011) 11–14.
- 853 [61] S. C. Hagen, J. J. Westerink, R. L. Kolar, One-dimensional finite ele-
854 ment grids based on a localized truncation error analysis, *International*
855 *Journal for Numerical Methods in Fluids* 32 (2000) 241–262.
- 856 [62] J. J. Becker, D. T. Sandwell, W. H. F. Smith, J. Braud, B. Binder,
857 J. Depner, D. Fabre, J. Factor, S. Ingalls, S. H. Kim, R. Ladner,
858 K. Marks, S. Nelson, A. Pharaoh, R. Trimmer, J. Von Rosenberg,
859 G. Wallace, P. Weatherall, Global bathymetry and elevation data at
860 30 arc seconds resolution: Srtm30plus, *Marine Geodesy* 32 (2009) 355–
861 371.
- 862 [63] M. Bilskie, S. Hagen, J. L. Irish, Development of return period stillwater
863 floodplains for the northern gulf of mexico under the coastal dynamics
864 of sea level rise, *J. Waterway, Port, Coastal, Ocean Eng.* 145 (2019)
865 04018043.
- 866 [64] M. Garland, P. S. Heckbert, Surface simplification using quadric error
867 metrics, in: *Proceedings of the 24th annual conference on Computer*

- 868 graphics and interactive techniques, ACM Press/Addison-Wesley Pub-
869 lishing Co., 258849, 1997, pp. 209–216.
- 870 [65] S. Jia, X. Tang, H. Pan, Fast Mesh Simplification Algorithm Based on
871 Edge Collapse, Springer Berlin Heidelberg, Berlin, Heidelberg, pp. 275–
872 286.
- 873 [66] N. Coll, M. Guerrieri, M.-C. Rivara, J. A. Sellars, Adaptive simplifica-
874 tion of huge sets of terrain grid data for geosciences applications, *Journal*
875 *of Computational and Applied Mathematics* 236 (2011) 1410–1422.
- 876 [67] P. L. George, F. Hecht, E. Saltel, Automatic mesh generator with speci-
877 fied boundary, *Computer Methods in Applied Mechanics and Engineer-*
878 *ing* 92 (1991) 269–288.
- 879 [68] P. L. George, E. Seveno, The advancing-front mesh generation method
880 revisited, *International Journal for Numerical Methods in Engineering*
881 37 (1994) 3605–3619.
- 882 [69] Aquaveo, Surface-water modeling system (2014).
- 883 [70] CPRA, 2017 Coastal Master Plan: Model Improvement Plan, Report,
884 The Water Institute of the Gulf, 2013.
- 885 [71] G. Egbert, A. Bennett, M. Foreman, Topex/poseidon tides estimated
886 using a global inverse model, *Journal of Geophysical Research: Oceans*
887 99 (1994) 24821–24852.
- 888 [72] G. Egbert, S. Erofeeva, Efficient inverse modeling of barotropic ocean
889 tides, *Journal of Atmospheric and Oceanic Technology* 19 (2002) 183–
890 204.
- 891 [73] M. Powell, S. Houston, L. Amar, N. LMorisseau-Leroy, The hrd real-
892 time hurricane wind analysis system, *Journal of Wind Engineering and*
893 *Industrial Aerodynamics* 77-78 (1998).
- 894 [74] A. Cox, J. Greenwood, V. Cardone, V. Swail, An interactive objective
895 kinematic analysis system, Alberta, Canada.
- 896 [75] E. Thompson, V. Cardone, Practical modeling of hurricane surface wind
897 fields, *Journal of Waterway, Port, Coastal, and Ocean Engineering* 122
898 (1996) 195–205.

- 899 [76] M. E. Luther, C. R. Merz, J. Scudder, S. R. Baig, J. L. T. Pralgo,
900 D. Thompson, S. Gill, G. Hovis, Water level observations for storm
901 surge, *Marine Technology Society Journal* 41 (2007) 35–43.
- 902 [77] J. C. Dietrich, A. Muhammad, M. Curcic, A. Fathi, C. N. Dawson,
903 S. S. Chen, R. A. Luettich, Sensitivity of storm surge predictions to
904 atmospheric forcing during hurricane isaac 144 (2018) 04017035.
- 905 [78] J. Gao, On the surface wind stress for storm surge modelling, Thesis,
906 2018.
- 907 [79] R. Cyriac, J. C. Dietrich, J. G. Fleming, B. O. Blanton, C. Kaiser, C. N.
908 Dawson, R. A. Luettich, Variability in coastal flooding predictions due
909 to forecast errors during hurricane arthur, *Coastal Engineering* 137
910 (2018) 59–78.
- 911 [80] J. Towns, T. Cockerill, M. Dahan, I. Foster, K. Gaither, A. Grimshaw,
912 V. Hazelwood, S. Lahtrop, D. Lifka, G. Peterson, F. Roskies, J. Scott,
913 N. Wilkins-Diehr, Xsede: Accelerating scientific discovery, *Computing
914 in Science and Engineering* 16 (2014) 62–74.